Centrifuge fractionation during purification of cellulose nanocrystals after acid hydrolysis and consequences on their chiral self-assembly

Svagan, Anna J.; Vilaplana, Francisco; Pettersson, Torbjörn; Anusuyadevi, Prasaanth Ravi; Henriksson, Gunnar; Hedenqvist, Mikael

DOI
10.1016/j.carbpol.2023.121723

Publication date
2024

Document Version
Final published version

Published in
Carbohydrate Polymers

Carbohydrate Polymers 328 (2024) 121723

Contents lists available at ScienceDirect

Carbohydrate Polymers

journal homepage: www.elsevier.com/locate/carbpol

Centrifuge fractionation during purification of cellulose nanocrystals after acid hydrolysis and consequences on their chiral self-assembly

Anna J. Svagan [a,*], Francisco Vilaplana [b,c], Torbjörn Pettersson [a], Prasaanth Ravi Anusuyadevi [a,d], Gunnar Henriksson [a], Mikael Hedenqvist [a]

[a] Royal Institute of Technology (KTH), Dept. of Fibre and Polymer Technology, Stockholm, Sweden
[b] Royal Institute of Technology (KTH), Dept. of Chemistry, Div. Glycoscience, Albanova University Centre, Stockholm, Sweden
[c] Royal Institute of Technology (KTH), Wallenberg Wood Science Centre (WWSC), Stockholm, Sweden
[d] Materials Science and Engineering Department (MSE), Faculty of Mechanical, Maritime and Materials Engineering (3mE), Delft University of Technology, 2628 CD Delft, the Netherlands

ARTICLE INFO

Keywords:
Cellulose nanocrystals
Fractionation
Structural colors
Sulfuric acid hydrolysis

ABSTRACT

The inherent colloidal dispersity (due to length, aspect ratio, surface charge heterogeneity) of CNCs, when produced using the typical traditional sulfuric acid hydrolysis route, presents a great challenge when interpreting colloidal properties and linking the CNC film nanostructure to the helicoidal self-assembly mechanism during drying. Indeed, further improvement of this CNC preparation route is required to yield films with better control over the CNC pitch and optical properties. Here we present a modified CNC-preparation protocol, by fractionating and harvesting CNCs with different average surface charges, rod lengths, aspect ratios, already during the centrifugation steps after hydrolysis. This enables faster CNC fractionation, because it is performed in a high ionic strength aqueous medium. By comparing dry films from the three CNC fractions, discrepancies in the CNC self-assembly and structural colors were clearly observed. Conclusively, we demonstrate a fast protocol to harvest different populations of CNCs, that enable tailored refinement of structural colors in CNC films.

1. Introduction

Cellulose nanocrystals (CNCs), which are semi-crystalline cellulose-based nanorods mainly derived from plant resources, possess the ability to self-assemble into chiral nematic structures, a property that has diligently been used in the past to produce structurally colored films. When the pitch (the full turn length of the CNC helix) of the nano-architecture is on the order of hundreds of nanometers, Bragg's reflection gives colors within the visible range, when incoming light interacts with the nanostructure (Revol, Bradford, Giasson, Marchessault, & Gray, 1992). Examples of brilliant structural colors are plentiful in nature, such as animals or fruits and leaves of plants (Graham, Lee, & Norstog, 1993; Hamidjaja, Capoulade, Catón, & Ingham, 2020; Moyroud et al., 2017; Vignolini et al., 2012). Practical advantages with structural colors are that they are non-bleaching, additionally, the nontoxic cellulose-based structural colors found in plants offer a sustainable alternative to colors originating from synthetic dyes, pigments and metals.

For CNC derived structural colors, the chiral nematic nano-ordering in films is attained through liquid, often water, removal from a suspension of CNCs, e.g. evaporation-induced self-assembly (EISA) of cellulose nanocrystals. During the drying, the CNCs enter a kinetically arrested "gel-like" state that locks the CNC ordering in place within the remaining time of the water removal (Lagerwall et al., 2014). In its kinetically arrested state, the CNC gel (or glass) displays solid-like character and does not flow in inverted cuvettes (Nordenström, Fall, Nyström, & Wågberg, 2017; Schütz et al., 2020; Tanaka, Meunier, & Bonn, 2004). This kinetic arrest is crucial in the development of colorful cellulose films and needs to set in at a CNC mass fraction where the liquid crystalline order is observed in the sample (Schütz et al., 2020).

Since its first report in the 1950s (Nickerson & Habrle, 1947; Rånby & Ribi, 1950), the sulfuric acid hydrolysis protocol still remains the most common method to isolate CNCs that are used for the preparation of materials with structural colors. Using strong sulfuric acid hydrolysis, the amorphous regions of the starting cellulosic materials can be removed and the resulting cellulose nanocrystals attain a negative surface charge, due to -OSO_3^- groups. The sulfate half ester groups provide the needed colloidal stability in suspension that is required for the self-assembly to take place, and the amount of groups must be high enough,

* Corresponding author.
E-mail address: svagan@kth.se (A.J. Svagan).

https://doi.org/10.1016/j.carbpol.2023.121723
Received 14 September 2023; Received in revised form 8 December 2023; Accepted 18 December 2023
Available online 20 December 2023

as insufficiently charged CNCs rather leads to flocculation or sedimentation (Beck & Bouchard, 2014; Camarero Espinosa, Kuhnt, Foster, & Weder, 2013). The conditions during the hydrolysis; sulfuric acid concentration, time, temperature and cellulose source, have previously been investigated and shown to influence morphology (shape), aspect ratio, degree of crystallinity and surface charge of CNCs (Bondeson, Mathew, & Oksman, 2006; Dong, Revol, & Gray, 1998; Elazzouzi-Hafraoui et al., 2008; Hamad & Hu, 2010). It is well-known that the derived CNC population in suspension will be highly polydisperse in size, shape and, potentially surface charge. This dispersity creates problems when materials with uniform properties are pursued. For example, the onset of the liquid crystal formation will depend on factors such as the aspect ratio of the CNCs (Honorato-Rios et al., 2018; Honorato-Rios & Lagerwall, 2020) and ionic strength (Dong, Kimura, Revol, & Gray, 1996). Recently Honorato-Rios et al. (2018) and Honorato-Rios and Lagerwall (2020) fractionated CNCs into shorter and longer CNCs using a fractionation method based on Onsager theory (Onsager, 1949), which states that long rods are ordered first into a birefringent liquid crystal phase that separates, due to gravity, from the isotropic phase containing shorter rods. Compared to shorter CNCs, the onset (≈3 wt% for long) and the fully developed cholesteric phase (≈6 wt%) were noted to occur earlier for the longer CNCs, although no change was found for the onset mass fraction at kinetic arrest (≈12 wt%). The last was contrary to what was expected, as kinetic arrest should occur earlier for longer CNCs (Honorato-Rios et al., 2018). The authors concluded that this was probably due to the insufficient aspect ratio for longer CNCs. Fractionation based on phase separation has also been performed by Dong et al. (1996, 1998) and additional reported fractionation strategies include centrifugation (Bai, Holbery, & Li, 2009) or centrifugation in a sucrose gradient (de Souza Lima & Borsali, 2002). However, in all these cases the fractionation was performed on already prepared CNC suspensions.

Another strategy, investigated here, is to fractionate the CNCs immediately after the sulfuric acid hydrolysis step, that is, during the centrifugation purification step. In this way we sort CNCs, by exploiting the ionic strength of the medium to sediment CNCs more easily. The hydrolysis is most often stopped by dilution with water and/or the CNCs are purified by centrifugation followed by discarding the supernatant and redispersion of CNCs in ultrapure water and then repeating these steps again (Araki, Wada, Kuga, & Okano, 2000; Bouchard, Méthot, Fraschini, & Beck, 2016; Gray & Mu, 2015; Hamad & Hu, 2010). Typically, the purification is stopped after a fixed number of repetitions, or when the supernatant becomes turbid (Bondeson et al., 2006; Gray & Mu, 2015). In some cases, however, centrifugation is omitted completely (Calvo et al., 2023). Afterwards, the CNCs are collected and further purified using dialysis. Post-processing of CNCs, to disperse nanorods, include e.g. (high-energy) tip sonication and/or filtration to break or remove larger CNC aggregates that intervene with the CNC assembly and structural color formation (Abitbol, Kam, Levi-Kalisman, Gray, & Shoseyov, 2018; Beck, Bouchard, & Berry, 2011; Bouchard et al., 2016; de Souza Lima & Borsali, 2002; Elazzouzi-Hafraoui et al., 2008; Schütz et al., 2020; Tran, Hamad, & MacLachlan, 2018; Xiong et al., 2020). Unfortunately, there is no unified CNC-production protocol in literature, hence, depending on the centrifugation protocol (relative centrifugal force, time and repetitions), the purification step will vary and as a result this may further add to the heterogeneity of the CNC size and charge population. Indeed, the resulting CNCs may constitute of a polydisperse population and this will influence the material's optical appearance and induce variations in the CNC pitch (Honorato-Rios & Lagerwall, 2020). Also, post-processing steps such as ultrasonication might yield shorter CNCs (Metzger, Drexel, Meier, & Briesen, 2021), damage potential chiral dopants (Parton et al., 2022) and more material than anticipated might be lost during filtration. As we will show in the present study, some of the potentially discarded supernatants during the hydrolysis purification step (the centrifugation step) actually contain very fine CNCs that can be used to create photonic/structurally colored materials. Additionally, such CNC supernatants are able to self-assemble into structural colored films, without any need of harsh post-processing conditions. Thus, the focus herein is on CNCs that can be fractionated already during the centrifugation purification step, by utilizing the ionic strength of the medium during sorting. The CNCs were extracted from microcrystalline cellulose (MCC) (Bondeson et al., 2006; Elazzouzi-Hafraoui et al., 2008), which is a pure cellulose source. The different CNC fractions were characterized with respect to size, aspect ratio and surface charge. A neutral molecule, glucose, was added to the different CNC fractions and the derived structural colors were evaluated.

2. Experimental part

2.1. Materials

Microcrystalline cellulose (MCC) Avicel® PH-200 was purchased from DuPont. Oligosaccharide standards (cellobiose, cellotriose, cellotetraose, cellopentaose, cellohexaose) were purchased from Megazymes (Ireland). D-(+)-Glucose (purity≥99.5 %), sulfuric acid (95–97 %), dinitrosalicylic acid (DNS), sodium potassium tartrate ($NaKC_4O_6{\cdot}4H_2O$), phenol, sodium sulfite (Na_2SO_3) and polyethylenimine (PEI, branched, Mw 25,000) were purchased from Sigma Aldrich/Merck.

2.2. Modified CNC preparation protocol

Preparing different fractions of CNCs: MCC (20 g) was hydrolyzed in sulfuric acid (247 g of 64 wt%) at 45 °C (temperature inside hydrolysis vessel) for 75 min. The sulfuric acid was preheated to 45 °C under magnetic stirring and MCC was added followed by 1 min of overhead stirring (ca. 200 rpm, PTFE centrifugal stirrer shaft) to remove MCC lumps. Because the magnetic mixing slowed down significantly in the presence of MCC (ca. 0–60 rpm), the overhead mixing was repeated for 1 min at the timepoints 10, 30, 45 and 70 min. In between timepoints, the shaft was removed and the hydrolysis proceeded in a closed flask. We note that intensified stirring during hydrolysis might yield other end results. The reaction was stopped by diluting 10-fold with MilliQ water and the suspension was left to settle overnight. The ionic strength at this point is on the order of approximately 2 M. The next day the upper supernatant (≈1.4 L) was removed and the entire sediment (600 mL in a 2 L plastic jug, 12 cm in diameter) was ultrasonicated for 2 min at 70 % followed by 2 min at 90 % amplitude (total energy of 30 J mL^{-1}, 1/2-inch tip placed ca. 0.5 cm from bottom, Vibra-Cell VCX 750, Sonics & Materials), followed by centrifugation at 16,000 rpm (rcf = 26,964*g*, 40 mL centrifuge vials, SORVALL RC 5B PLUS centrifuge, Fiberlite F21-8 × 50y rotor) for 5 min and then the remaining supernatant was rejected. The ultrasonication of the 600 mL suspension, was done to disperse aggregates prior to centrifugation, but at the same time we kept the energy input low (30 J mL^{-1}) not to shorten CNCs significantly. The effect of ultrasonication depends on sample volume and beaker size (Girard, Vidal, Bertrand, Tavares, & Heuzey, 2021). The sediment (after centrifugation) was diluted with MilliQ water to the same volume (sediment was diluted ca. 10-fold with MilliQ water each time) as prior to the centrifugation and dispersed by shaking the vials using a vortex mixer (Vortex-Genie 2). The centrifugation/redispersion-step with vortex mixer was repeated. After the third centrifugation (three centrifugations performed in total), the supernatant was instead collected as CNC-H fraction No 1. The sediment was dispersed again and the vials were centrifugated for 10 min. Afterwards, the supernatant was collected as CNC-H fraction No 2 and the sediment is denoted CNC-H fraction No 3. The CNC-H fraction No 3 was diluted with MilliQ water. Each fraction was dialyzed separately (cellulose membrane tube, 14 kDa molecular weight cut-off, the surrounding 3 L MilliQ water replaced 2 times per day, except the second and third day, when it was replaced once) until the pH of the surrounding water was stable (7 days). The concentrations, pHs and amounts of the retrieved CNC-H fractions were; 0.43 wt% (No 1, pH = 3.0, 480 g), 0.64 wt% (No 2, pH = 2.9, 400

g) and 2.64 wt% (No 3, pH = 2.5, 180 g). The total CNC yield was 47 % (with respect to the 20 g MCC initially used). For each CNC fraction, the yield was 10 % (No 1), 13 % (No 2) and 24 % (No 3). The amount of sulfate half-ester groups (R-OSO_3H, mmol/g) and hence the surface charge was evaluated by conductimetric titration as described elsewhere (Reid, Villalobos, & Cranston, 2017), using a 4 mM NaOH solution as the titrant. Here, an amount of 1–6 mL of CNC suspension was added to 70 mL 1 mM NaCl.

2.3. Preparation of CNC/GLU films

D-(+)-Glucose (GLU) was added to glass vials (40 mL) containing different amounts of CNC-H suspensions (concentrations of 0.43 wt%, 0.64 wt% or 2.64 wt% for No 1, No 2 and No 3, respectively) to prepare films with CNC/GLU compositions ranging from 58/42 to 100/0. As a comparison, a vial containing a mixture of CNC-H fractions No 1, No 2 and No 3 in their original proportions (No 1:No 2:No 3 = 2.7:2.2:1) was also prepared. The total dry content of the CNC-H/GLU suspensions was ca. 100 mg (films prepared using CNC-H fractions No 1 or No 2 or No 1/No 2/No 3 mixture) or ca. 160 mg (films, CNC-H fraction No 3). To dissolve and disperse the CNCs and glucose, the different suspensions were first subjected to magnetic mixing over-night, followed by 60 min of sonication treatment of the suspensions, still present in the vials, at 30 °C in an ultrasonic water bath (Branson CPX2800H-E, ultrasonic water bath, 2.8 L, 110 W, 40 kHz). The (mild) ultrasonic bath treatment is central to obtaining a good dispersion. Note that the ultrasonic bath step employed here was gentler (see resulting CNCs in our DLS and AFM results) than the more energy-intense tip-ultrasonic processing conditions reported in literature, that shorten and delaminate CNCs (Beck et al., 2011; Parton et al., 2022). The suspensions were cast on polystyrene Petri dishes (bottom diameter; 5.2 cm). The films were dried inside a storage cabinet (ca. 80 × 80 × 27 cm, cabinet door opened ca. 3 cm) at 20–30 %RH and 19 ± 0.9 °C (for 100/0 No 1/No 2/No 3 mixture; ca. 30 %RH and 19 ± 1 °C) over a period of 1–2 weeks.

2.4. Dynamic light scattering

The hydrodynamic radius and translational diffusion coefficient were measured using dynamic light scattering (Zetasizer Pro ZSU3205, Malvern Instruments). Prior to analysis all suspensions (No 1, No 2 and No 3) were first magnetically stirred overnight, diluted to a volume fraction between 6×10^{-4} to 6×10^{-5} and then sonicated (Branson CPX2800H-E, ultrasonic 2.8 L water bath) at 30 °C for 60 min, to mimic CNC/GLU film preparation conditions.

The length of the CNC-Hs (L) was calculated from the average cross-section (d) of the CNC-H (obtained via AFM) and the translational diffusion coefficient (D_t) was obtained for CNC-H rods (volume fraction ca. 6×10^{-5}) in a 1 mM NaCl suspension, as described earlier (Nordenström et al., 2017). The length was calculated from (de la Torre & Bloomfield, 1981);

$$\frac{3\pi\eta L D_t}{k_B T} = ln\frac{L}{d} + c_0 + c_1\frac{d}{L} + c_2\left(\frac{d}{L}\right)^2 \quad (1)$$

where η is the viscosity of the solvent, k_B is Boltsmann's constant and T is the temperature. The constants, $c_0 = 0.312$, $c_1 = 0.565$ and $c_2 = 0.1$, apply when modelling random translation diffusion of cylinders in solution (de la Torre & Bloomfield, 1981).

2.5. Atomic force microscopy (AFM)

Imaging CNC-H fractions, deposited on polished silicon wafers, was performed using a MulitMode 8 (Bruker, Santa Barbara, CA) in PeakForce QNM mode using ScanAsyst cantilevers (Bruker, Camarillo, CA). The silicon wafers were first treated by adsorbing a layer of PEI (0.01 wt % PEI solution, 1 min exposure time), followed by rinsing with MilliQ-water and drying with a flow of filtered nitrogen gas. Then a drop of the CNC-H suspension (0.004 wt% suspension or further diluted to 0.0014 wt% suspension) was deposited on the wafer, followed by immediate rinsing (MilliQ-water) and drying with a flow of filtered nitrogen gas. All CNC-H suspensions (0.004 wt%) were magnetically stirred overnight, then sonicated (Branson CPX2800H-E, ultrasonic 2.8 L water bath) at 30 °C for 60 min prior to use. The AFM software Gwyddion (version 2.63) was used to measure the cross-sections (heights) and lengths of CNCs.

2.6. Polarized optical microscopy (POM)

POM images, using crossed linear polarizers in reflection mode, were obtained with a Leica DM750M microscope equipped with a Leica ICC50W camera and 10× and 20× Pol objectives.

2.7. UV–vis spectrometry

Spectra in direct transmittance were obtained using a UV–vis spectrophotometer (Shimadzu UV 2550). Prior to measurement the films had been conditioned at 50 %RH and 22 ± 1 °C for one day.

2.8. Inverted cuvette test

CNC-H suspensions were magnetically stirred overnight, sonicated (Branson CPX2800H-E, ultrasonic 2.8 L water bath) for 1 h at 30 °C and concentrated to ca. 4.2–4.5 wt% by water evaporation at 40 °C. The suspensions were poured into rectangular polystyrene cuvettes (1.2 × 1.2 cm^2, see Fig. 3e) and then further slowly concentrated (to 5–5.3 wt %) at ambient conditions until the cuvettes could be inverted for 24 h, without the interior CNC suspension starting to flow (Nordenström et al., 2017; Schütz et al., 2020).

2.9. Suspension between crossed linear polarizers

Linear polarizer films (Film Polarizers, 400–700 nm, Thorlabs) were mounted 90° to each other at a 17.5 cm distance, and all sides (except polarizer films) were covered to block out light. The distance from the cuvettes to the front linear polarizer was 15.5 cm. CNC-H suspensions were magnetically stirred overnight, concentrated to the right concentration (ca. 2, 3 or 4 wt%) by water evaporation at 40 °C and sonicated (Branson CPX2800H-E, ultrasonic 2.8 L water bath) at 30 °C for 60 min. In the case of CNC-H fraction No 3, the suspension was concentrated at 40 °C from 2.6 wt% to 5.2 wt% and then diluted to the right concentrations. The suspensions were poured into rectangular 10 mm quarts cuvettes (see Fig. 3a–d) and sealed with PTFE stoppers or lids, that were further wrapped with parafilm. To achieve slow drying inside some cuvettes (the two last cuvettes in Fig. 3a and b), PTFE lids and less parafilm was used (one turn), which allowed water to slowly escape over the investigated time period. The water-loss was 19 vol% (cuvette 3.6 wt %, Fig. 3b) and 19 vol% (cuvette 4.9 wt%, Fig. 3b), 24 vol% (cuvette 4 wt%, Fig. 3a) and 13 vol% (cuvette 4.6 wt%, Fig. 3a). All cuvettes were stored for 6 weeks.

2.10. Anion-exchange chromatography

Prior to measurements, the CNC-H suspensions (concentrations 0.43 to 0.88 wt%) were dispersed by magnetic stirring overnight, followed by 60 min of sonication at 30 °C (ultrasonic 2.8 L water bath, Branson CPX2800H-E). Afterwards, the CNCs were separated from the solution by filtrating the suspensions through a 0.45 μm PTFE syringe filter. The samples (20 μL) were injected into an anion-exchange chromatography system with pulsed amperometric detection (Dionex ICS5000, Thermo Fisher Scientific, USA) equipped with a 3 × 250 mm CarboPac PA200 analytical and a 3 × 50 mm CarboPac PA200 guard column (Thermo Fisher Scientific, USA). Separation of the cellooligosaccharides was

performed at a flowrate of 0.5 mL/min using a linear gradient from 30 mm NaOH to 30 mm NaOH/300 mm sodium acetate for 20 min and equilibration at the initial conditions for 10 min. Glucose and cello-oligosaccharide standards (external calibration) were used to detect and quantify their presence in the CNC-H suspensions. The reported values are presented as the average of three measurements.

2.11. Reducing end determination with DNS-reagent assay

Reducing sugar ends of CNC in MilliQ-water suspensions were estimated using a dinitrosalicylic acid (DNS) reagent assay (Saqib & Whitney, 2011). One liter of DNS reagent solution contained 10 g NaOH, 10 g of DNS, 100 g $NaKC_4O_6$, 2 g phenol and 0.5 g Na_2SO_3. The CNC-H suspensions were magnetically stirred overnight, then sonicated (Branson CPX2800H-E, ultrasonic 2.8 L water bath) at 30 °C for 60 min. Equal amounts DNS and CNC suspension or DNS and glucose solution were added in glass vials and sealed with a lid. All vials were simultaneously boiled for 20 min (water bath) and then transferred to ice for rapid cooling and finally brought back to room temperature and centrifuged (13.5k rpm, 3 min, microcentrifuge, Micro Star 12, VWR). The supernatants were collected and analyzed (absorbance at 575 nm) using a UV–vis spectrophotometer (Shimadzu UV 2550). The mixtures of glucose and DNS reagent were used to attain the calibration curve. The reported reducing sugar ends of CNCs are an average of three different measurements.

3. Results and discussion

3.1. CNC-H fraction

Using centrifugation, we fractionated CNCs after hydrolysis by exploiting the ionic strength of the medium during separation. In this way, we obtained three fractions of CNCs with different sizes, surface charges and with H^+ as counterions, as illustrated in Fig. 1a. The three fractions are here denoted as No 1, No 2 and No 3. Two of the CNC-H populations, No 1 and No 2 fractions, were present in the supernatant after centrifugation, whereas the third one was the sediment after the fourth centrifugation. As a result, the clarity of the three fractions differed significantly at the same concentration, here 0.4 wt% (≈0.3 vol %). The fraction No 3 suspension was opaque, whereas fractions No 1 and No 2 were translucent, see Fig. 1b. Our CNC-centrifugation protocol differs from the more commonly reported purification strategies in literature, in which sedimented CNCs are only collected, or, once the supernatant becomes turbid, both the supernatant and sedimented CNCs are collected as one sample (Bondeson et al., 2006). For the present centrifugation conditions, our suspension became turbid after the fourth centrifugation. Hence, if the turbidity protocol was applied here, this means that fraction No 1 (Fig. 1a) that was generated after the 3rd centrifugation, would never be collected. Likewise, fractions No 2 and No 3 would be collected as one polydisperse sample, or, only No 3 would be kept.

The amount of sulfate groups per mass CNC is included in Fig. 1c and the apparent size distribution from DLS for fractions No 1–3 is presented in Fig. 1d. Clearly, the fractions differed both in size and the average surface charge, that originates from the amount of sulfate half ester groups. The first two CNC fractions were similar in apparent size distribution, but varied in the amount of sulfate groups (average value of 0.446 versus 0.377 mmol/g CNC). CNC fraction No 3 had larger CNC aggregates present, Fig. 1d. When compared to the other two fractions, the surface charge was the lowest for fraction No 3 (0.296 mmol/g CNC). Still, this is a value comparable to that of commercial CNCs (ca. 0.200–0.330 mmol/g) (Reid et al., 2017).

In Fig. 2a–c, AFM micrographs of the different CNC-H fractions are presented. As expected, fraction No 3 contained large-sized fiber fragments, but also finer CNCs comparable to those found in fraction No 2, see Fig. S1 in SI. CNC-H fractions No 1 and No 2 were similar on average in width, length and aspect ratio, see histograms in Fig. 2d–f. Average cross-section sizes (d) of CNC-H were 7.1 ± 1.9 nm (No 1) and 6.6 ± 2.3 nm (No 2), average CNC-H lengths (L) were 350 ± 170 nm (No 1) and 270 ± 130 nm (No 2), with corresponding average aspect ratios (L/d) of

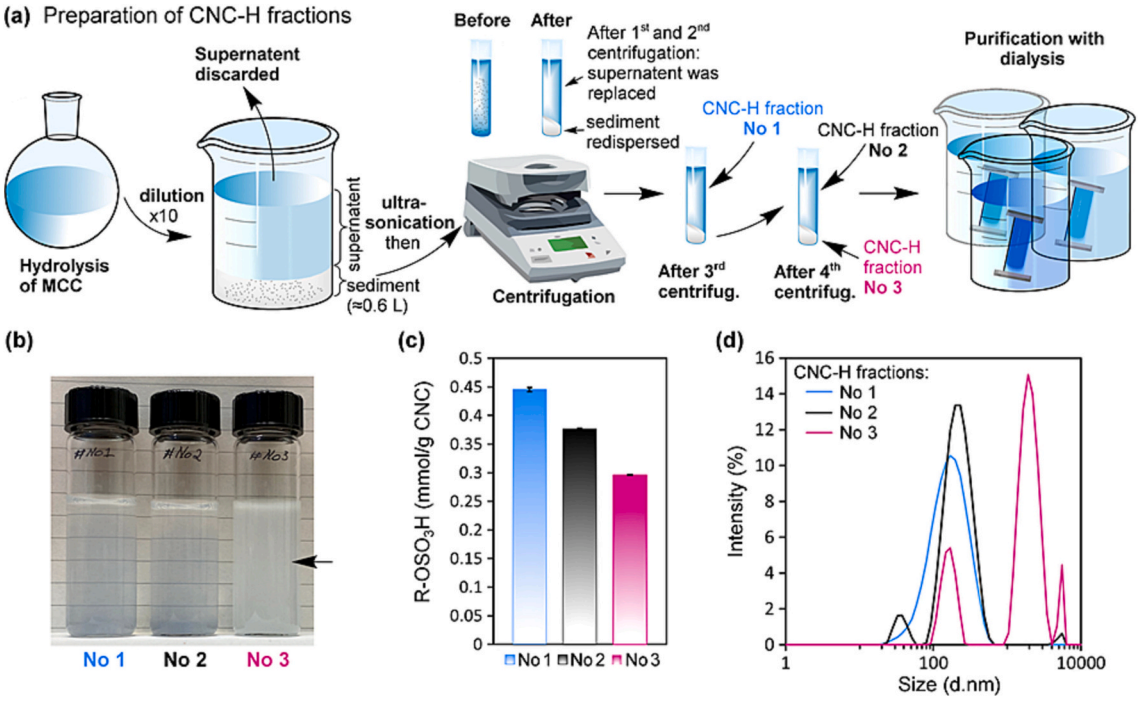

Fig. 1. (a) Schematic of different steps in CNC-H preparation. The different CNC-H fractions (No 1, No 2 and No 3) were collected after centrifugation and the fractions were dialyzed separately. (b) At 0.4 wt% CNC-H concentration, both No 1 and No 2 fractions appeared translucent whereas the No 3 fraction was opaque. As pointed out with the black arrow, the background is not visible for No 3. Glass vial width; 2.1 cm. (c) The number of sulfate half ester groups per mass of CNC decreased with CNC-H fraction No 1 to No 3. (d) DLS results for the different dilute CNC-H fractions.

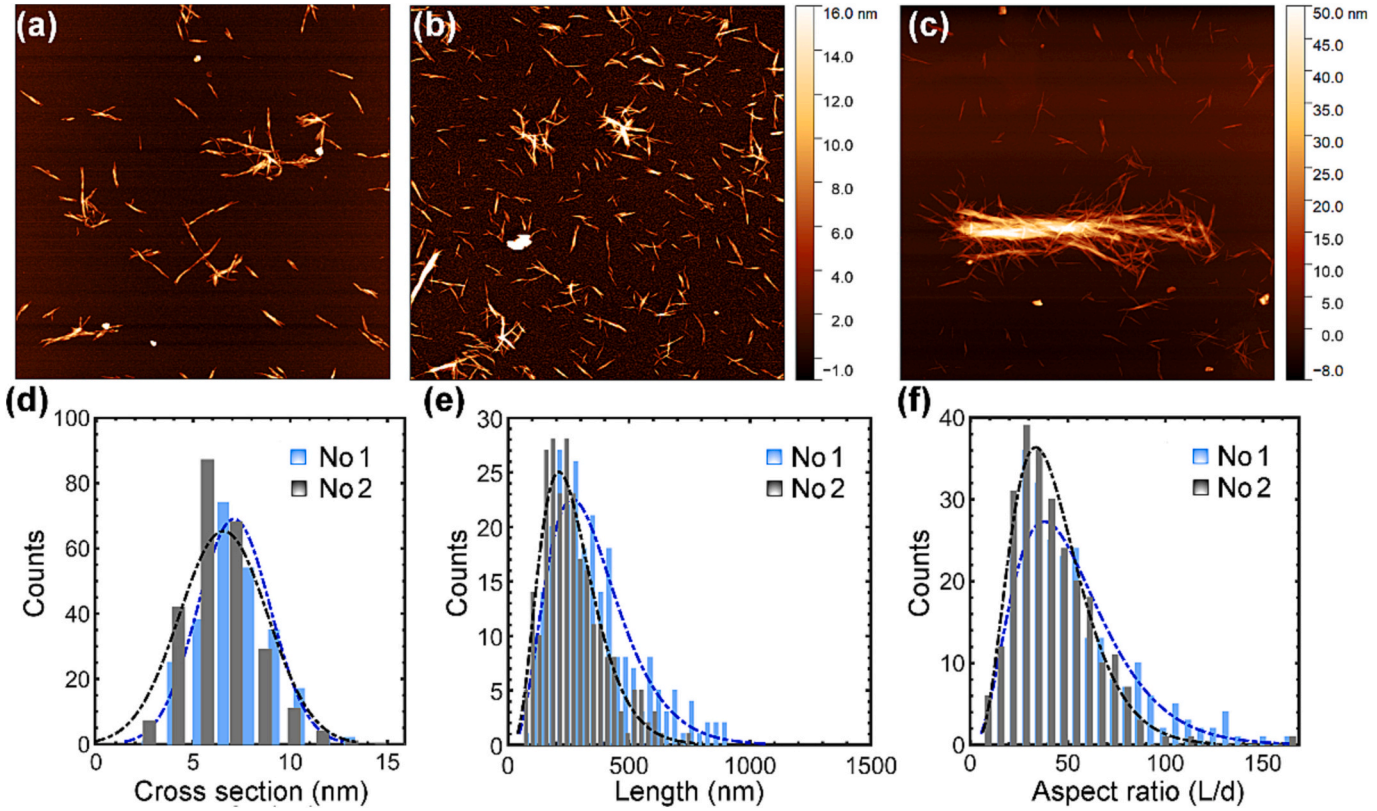

Fig. 2. AFM micrographs of the CNC-H fractions (a) No 1 (b) No 2 and (c) No 3. AFM micrographs were 5 × 5 μm in size. Histograms showing the (d) CNC-H cross section, *d*, (e) CNC-H length, *L*, and (f) aspect ratio, *L/d*, of CNC-H fractions No 1 and No 2. The dotted lines are either fitted normal distribution (d) or log-normal distribution curves (e–f).

51 ± 28 (No 1) and 43 ± 20 (No 2).

To disclose CNC-H lengths further, the translation diffusion coefficients (D_L) obtained from DLS were compared; 3.02 ± 0.16, 3.10 ± 0.02, and 0.34 ± 0.05 $\mu m^2\ s^{-1}$ (n = 3) for CNC-H fractions No 1, No 2 and No 3, respectively. The low diffusion coefficient for fraction No 3 suggests larger CNCs, whereas similar diffusion coefficients for fraction No 1 and No 2 corroborates with smaller CNCs of similar sizes. As it may be difficult to perfectly decipher CNC lengths from AFM micrographs, due to difficulties seeing where a CNC rod starts and ends, we also used Eq. (1) to compute the lengths from the D_L values. The average (and standard deviation) CNC length for No 1 and No 2 fractions were calculated to $L_{No1} = 830 \pm 60$ nm and $L_{No2} = 820 \pm 6$ nm, respectively. Interestingly, both CNC-H fraction No 1 and No 2 (both AFM and calculated from DLS) were longer than CNCs typically derived from wood-based microcrystalline cellulose (≈100–200 nm on average) (Bondeson et al., 2006; Elazzouzi-Hafraoui et al., 2008; Nordenström et al., 2017). Using the DLS derived CNC lengths, an aspect ratio (L/d) of ca. 100 was obtained for our CNCs.

The photographs, taken of the CNC-H suspension between crossed linear polarizers at different concentrations after 6 weeks of storage, are included in Fig. 3. The separation into an upper and lower phase observed for CNC-H fraction No 3 (Fig. 3c) during unperturbed storage is typical, and reported as an upper isotropic and lower cholesteric phase for CNC suspensions prepared by the traditional manufacturing protocol (Parker et al., 2018). Here, because fraction No 3 contained both aggregates, but also finer CNCs (AFM images Figs. 2c and S1), we hypothesize that the lower part in Fig. 3c is a mixture of a cholesteric phase and sedimented aggregates (due to size). Also, that the separation took place at relatively low weight %, here concentrations up to only 3 wt% studied, is typically observed for longer CNCs, see reference (Honorato-Rios & Lagerwall, 2020). More interestingly, the same phase separation dynamics was absent for the CNC-H fractions No 1 and No 2, Fig. 3a and b. These cuvettes were exposed to two different scenarios; the suspensions containing up to 3 wt% CNCs were stored unperturbed for 6 weeks, whereas the two last cuvettes in Fig. 3a or b were also very slowly concentrated through slow evaporation of water in situ. For the last cuvettes, a volume reduction of around 20 vol% took place over the entire 6 weeks period, as exemplified in Fig. 3d. From Fig. 3a–b and d we see that as the CNC-H concentration increased, the birefringence properties changed, from a homogenous appearance (concentrations up to ca. 3 wt%), followed by an irregular and finally a more regular birefringent pattern as a sign of a long-range orientational CNC-H rod order. The investigated average concentrations were all below the kinetic arrest concentration (ca. 5 wt%, Fig. 3e). Surprisingly, any tactoids present in CNC-H fractions No 1 and No 2 did not appear to sediment (due to gravity) and merge at the bottom of the cuvette (Wang, Hamad, & MacLachlan, 2016). That tactoids can remain in the isotropic phase over longer time periods (months), has been reported previously (Honorato-Rios & Lagerwall, 2020). The phase transition of CNCs with larger aspect ratios, can also follow a slow spinodal decomposition, which involves anisotropic phase formation due to density fluctuations (Parker et al., 2018).

In Fig. 3d, the re-arrangement of CNC-H fraction No 2 was monitored with time as the suspension was gradually concentrated from 4.0 wt% (t = 0) to 4.9 wt% over a time-period of 42 days. CNCs stick to untreated glass surfaces (Mu & Gray, 2014), hence as water evaporated, an edge-effect (see black arrows shown in "11 days" cuvette in Fig. 3d) developed with time due to radial strain (Dumanli et al., 2014), favoring CNC alignment (Pullawan, Wilkinson, & Eichhorn, 2013) and a birefringent pattern formation. The re-organization of CNC-H propagated from the edges to the middle and lower part of the cuvette with time. In related experiments, Araki et al. (Araki et al., 2000) made colorful birefringent pattern observations when studying very fine CNCs in suspension at steady state made from a modified two-step hydrolysis protocol (HCl,

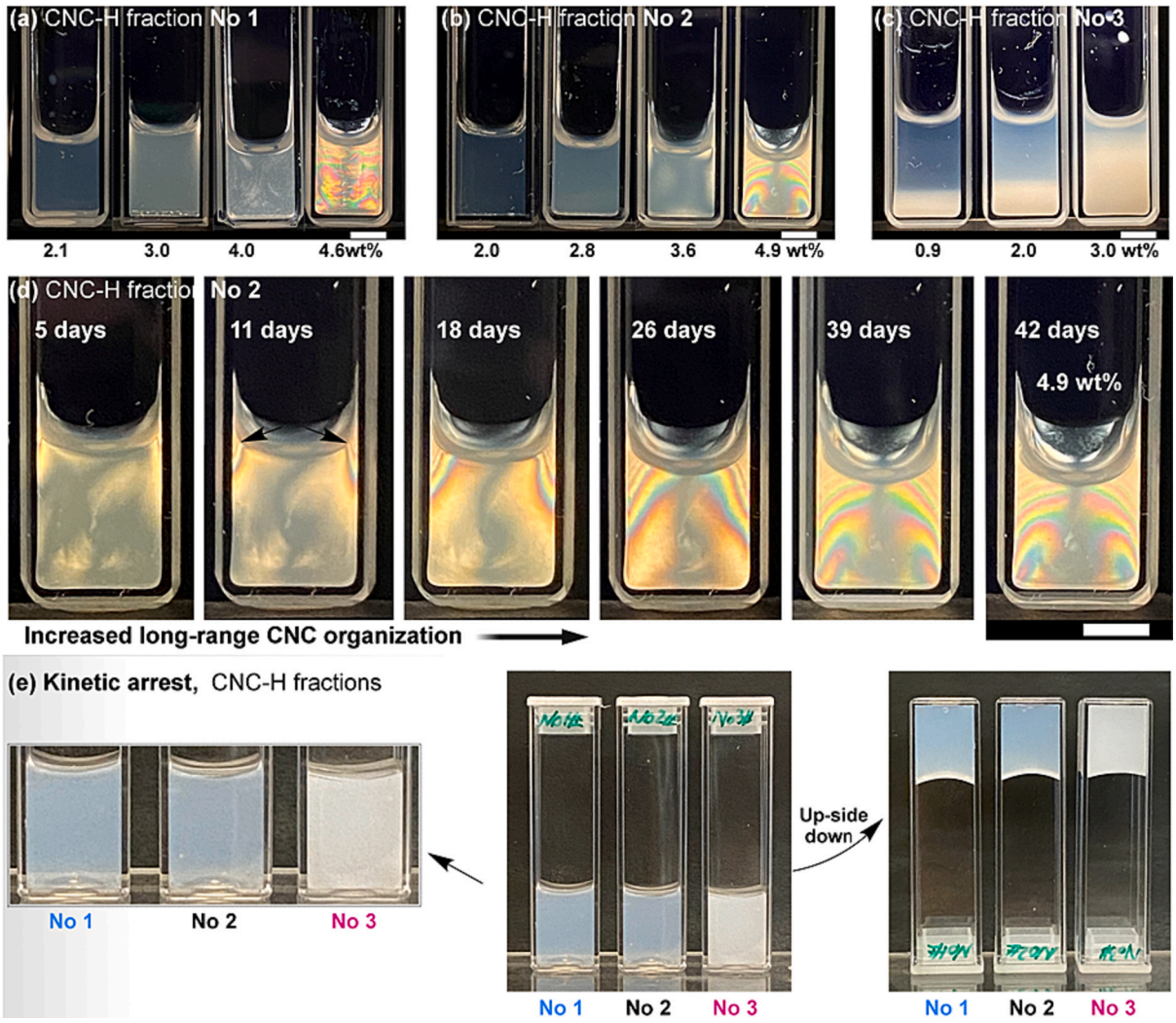

Fig. 3. Photos of CNC-H suspensions between crossed linear polarizers containing CNC-H fractions; (a) No 1, (b) No 2 and (c) No 3. Suspensions were stored for 6 weeks prior to imaging. (d) Rearrangement of CNCs (CNC-H fraction No 2) during slow evaporation of water for 42 days. CNC concentration was 4 wt% at t = 0. (e) Non-polarized photos of inverted cuvettes containing CNC-H fractions No 1–3 to demonstrate kinetic arrest at a concentration of ca. 5 wt%. The cuvette width; 12 mm (e). Scale bars; 5 mm (a–d).

then H_2SO_4 hydrolysis) or just after shearing a dilute suspension of high aspect ratio bacterial CNCs (Araki & Kuga, 2001), which temporarily oriented the crystals. In the first study, at a CNC content of 7.1 wt%, they observed a colored birefringent pattern for the suspension when viewed between linear crossed polarizers. Here, an even more apparent long-range arrangement of CNCs (No 2 and No 1, Fig. 3b and a) was detected, in particular for CNC-H fractions No 2 at the highest concentration (4.9 wt%). For this sample, the distinct color stripes reappeared in a periodic manner with height. This birefringent pattern is a consequence of a long-range alignment of CNCs in suspension (Tatsumi, Teramoto, & Nishio, 2015). CNC rods in suspension have been reported to tend to connect in chains (end-to-end) forming supra rods near the kinetic arrest concentration (Schütz et al., 2020). A helical CNC arrangement was also likely simultaneously present in the repeating rainbow color texture, with the helical axis in the direction of the height of the CNC suspension pillar. A cholesteric order in a repeating color pattern has previously been reported (Mu & Gray, 2014). Note that the linear polarizer (in front of the cuvette) removes light emerging from the cuvette at wrong angles, and in the absence of the polarizer, the suspensions were "colorless", as in the non-polarized photos of CNC fractions in plastic cuvettes in Fig. 3e.

The kinetic arrest for the three suspensions (tested using the 24 h inverted cuvette test) occurred between 5 and 5.3 wt%, with fraction No 3, having the lowest concentration of 5.0 wt% at kinetic arrest, Fig. 3e. For fractions No 1 and No 2 the concentrations were comparative and slightly higher at 5.3 wt% and 5.2 wt%, respectively. Still, both fraction No 1 and No 2 were more translucent when compared to No 3, see close-up in Fig. 3e, indicative of less aggregates present in fractions No 1 and 2. The concentrations at kinetic arrest at ca. 5 wt% are relatively low compared to previously noted kinetic arrest at ca. 12 wt% (Honorato-Rios et al., 2018), a difference that could be explained by that the present CNCs are longer and have a higher surface charge. At the kinetic arrest the counterion (H^+) concentration (C_{H^+}) was 23.6 mM (fraction No 1), 19.6 mM (fraction No 2) and 14.8 mM (fraction No 3). Here the amount of counterions was estimated from titration, hence the concentration of free H^+ (i.e. not surface condensed) is expected to be smaller. Still, with these H^+ values, the lower limit of the Debye screening length can be obtained. The counterion concentrations corresponded to a lower limit of Debye screening lengths ($\kappa^{-1} = 0.43/\sqrt{C_{H^+}(M)}$ nm at 20 °C, only counterions in equation (Israelachvili, 2010)) of $\kappa^{-1} = 2.8$ nm (fraction No 1), 3.1 nm (fraction No 2) and 3.5 nm (fraction No 3). At these counterion concentrations, it has been suggested that mobility constraints are more important than aggregation due to counterions (Nordenström et al., 2017), i.e. the

kinetically arrested CNC-H suspensions in Fig. 3e are likely colloidal glasses.

3.2. Structural colors derived from different CNC fractions

Iridescent films with various structural colors were realized here by casting blends of CNCs and D(+)-glucose (GLU) in different ratios. Glucose was selected as it does not change the ionic strength in solution. Previous studies have shown that D(+)-glucose influences the equilibrium pitch in the dry state (Anusuyadevi et al., 2021; Anusuyadevi et al., 2023; Mu & Gray, 2014), potentially with glucose acting as a chiral dopant, that improves the helical twisting power of CNCs (by lowering the internal energy barriers for rotation). The D(+)-glucose molecule is chiral and rotates transmitted plane polarized light to the right (dextrorotatory). Mixing glucose with CNC-H has been reported to decrease the pitch (blue-shift) in suspension (best observed at low glucose contents), although when dried down a red-shift in color was obtained (Mu & Gray, 2014). Here, to achieve blue and red iridescent colored films, we added an increasing weight fraction of glucose to the CNC-H suspensions. After the evaporation step, iridescent films were successfully retrieved from CNC-H fractions No 1 and No 2 (Fig. 4a–d), whereas structural colors were absent for the No 3 fraction films, see Fig. 4e–f. Moreover, no structural color was observed in a neat CNC-H film (100/0) based on a mixture of fraction No 1, No 2 and No 3 in their original proportions, see Fig. 5. In that case, the direct transmittance spectrum was very similar to that of fraction No 3 (100/0 film, Fig. 4f). Photographs of the remaining films not presented in Fig. 4 are found in Figs. S2 and S3 in SI. The visual observations were further supported by each film's direct transmittance spectra, Figs. 4b, d, f and 5b. Remarkably, when comparing films with similar CNC/GLU compositions and made from fraction No 1 (Fig. 4b) or No 2 (Fig. 4d), a clear blue-shift in color was observed for the CNC-H No 1 fraction-based films. The positions of the dips in the direct transmittance spectra for films based on CNC-H fraction No 2 (CNC/GLU: dip position, 100/0: 410 nm, 89/11: 420 nm, 67/33:780 nm and 58/42: IR-region), were blue-shifted for films with similar CNC/GLU compositions, but based on CNC-H fraction No 1 (100/0: UV-region, 88/12: 350 nm, 68/32: 640 nm and 58/42: 720 nm). The thicknesses of films were 30–41 μm (CNC-H No 3 films), 20–24 μm (CNC-H No 2 films) and 18–25 μm (CNC-H No 1 films).

The evaporation-induced-self-assembly of CNCs into films depends both on attractive (van der Waals forces, hydrogen bonds) and repulsive interactions (short-range and longer-range repulsions, steric or electrostatic) (Buining, Philipse, & Lekkerkerker, 1994; Evans & Wennerström, 1999; Israelachvili, 2010). The long-range repulsion scales with the Debye screening length, κ^{-1}, which is inversely proportional to the square root of the ionic strength of the medium and influences the self-organization of the CNCs (Schütz et al., 2020). Hence, the Debye length, κ^{-1}, decreases with higher ionic strength (I). The ionic strength, I, in turn, depends on the free ionic species in solution, which includes added ions and the counterions (here H^+) to the CNC charged -OSO_3^- groups, but not the -OSO_3^- groups bound to the surface of CNCs (Israelachvili, 2010). This implies that increasing the number of surface groups of CNCs, which introduces more counterions, increases the ionic strength (Schütz et al., 2020).

The absence of a structural color in CNC-H No 3 fraction-based films, and films based on the CNC-H No 1, No 2 and No 3 mixture (Fig. 5), was likely due to the CNC polydispersity in these samples, that is, the presence of large aggregates (DLS results in Fig. 1d and in AFM image Fig. 2) which did not allow the proper self-assembly into a chiral nematic

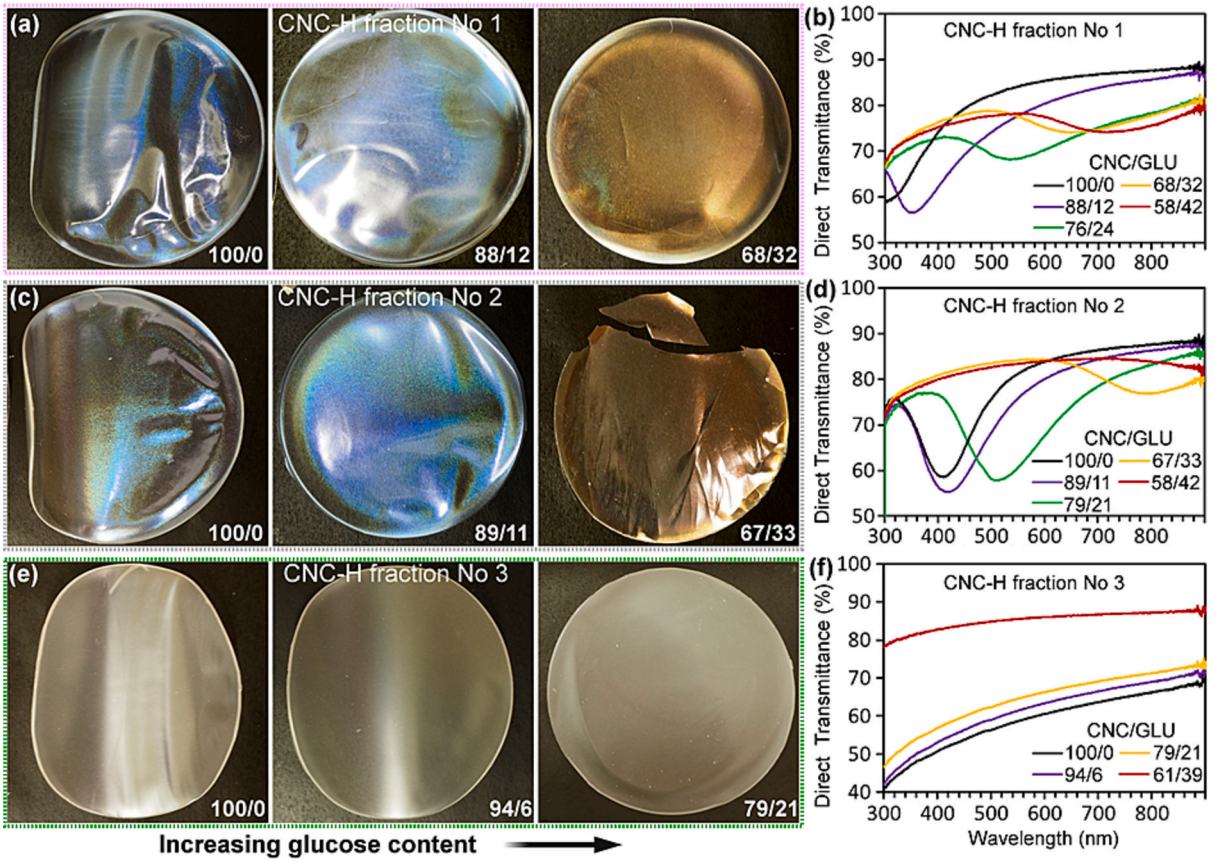

Fig. 4. Photographs and direct transmittance spectra of photonic CNC/GLU films made from fractionated CNCs and varying glucose (GLU) weight contents. CNC-H/GLU films using CNC-H fractions (a–b) No 1 (CNC/GLU = 100/0, 88/12, 76/24, 68/32 and 58/42), (c–d) No 2 (CNC/GLU = 100/0, 89/11, 79/21, 67/33 and 58/42) and (e–f) No 3 (CNC/GLU = 100/0, 94/6, 79/21 and 61/39). Spectra obtained for films equilibrated at 50 %RH and 22 °C.

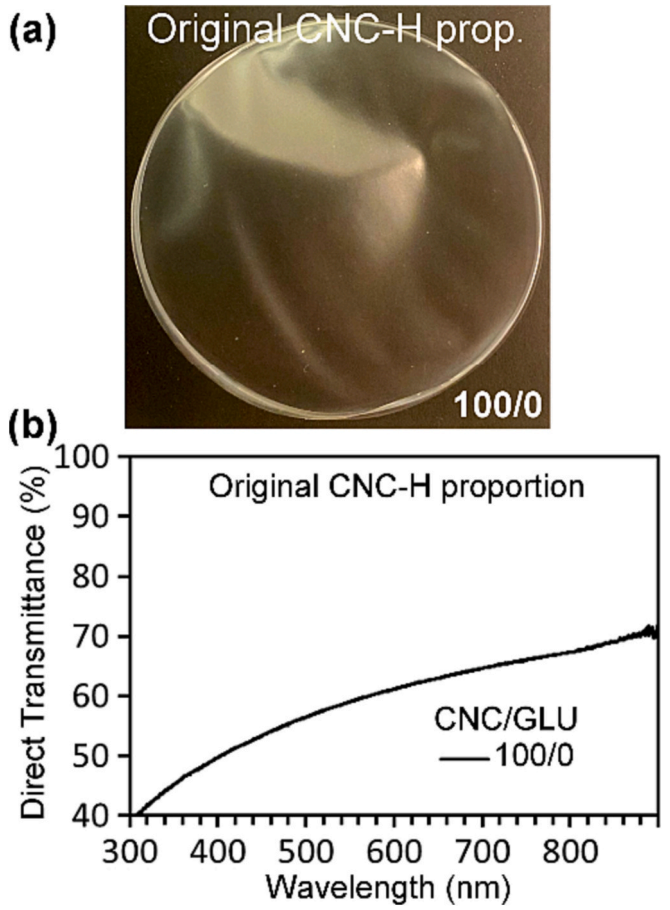

Fig. 5. (a) A photograph and (b) direct transmittance spectrum of a CNC/GLU film (CNC/GLU = 100/0) made from a blend of the CNC-H fractions No 1, No 2 and No 3. The fractions were mixed in their original proportions. Spectrum obtained for film equilibrated at 50 %RH and 22 °C.

structure. To successfully assemble fraction No 3, further post-processing is needed to break the remaining wood residues (Xiong et al., 2020), but that was not performed here. For films made from CNC-H fraction No 1, the difference to fraction No 2 based films with similar CNC/GLU compositions, is primarily due to the higher surface charge of CNC-H fraction No 1 (Fig. 1c). Note that both fractions had CNCs of similar average dimensions, see Fig. 2. Still, any influence of chiral features due to shape differences was not investigated here. The higher ionic strength, due to the presence of more counterions (H^+ species) (Schütz et al., 2020), reduces the Debye length, κ^{-1}, which decreases the effective nanorod volume and enables closer packing (Abitbol et al., 2018; Araki & Kuga, 2001). As a result, the pitch decreased and the structural colors (compare the dip-positions in the transmittance spectra for films based on fractions No 1 and No 2, Fig. 4) were blue-shifted for CNC/GLU films made from CNC-H fraction No 1.

The POM images in reflection-mode of different CNC/GLU films are shown in Fig. 6. The films with structural colors, that is all CNC/GLU films prepared from either CNC-H fraction No 1 or No 2, showed fingerprint patterns that are typical for CNCs arranged in a chiral nematic order. Upon closer look, several fingerprint pattern domain boundaries were simultaneously present, e.g. film 58/42 in Fig. 6b, which suggests incomplete merger and reorientation of different anisotropic domains during drying. In POM images of films which did not display structural colors, i.e. films made from the CNC-H fraction No 3, these fingerprint patterns were rare and occasionally detected in very tiny areas (Fig. 6c). Instead more often what appeared as Schlieren Patterns (in particular seen in CNC-H No 3/GLU = 79/21), present as dark lines between brighter domains, were observed.

The results in Fig. 3d validate that CNCs in fraction No 2 were able to orient themselves on longer length-scales and the same was observed in some areas of the films made from this fraction. As shown in the POM image in Fig. 7 of the CNC-H/GLU film (fraction No 2) with composition 79/21, the fingerprint pattern runs, more or less, in the same direction over the analyzed surface area. Additionally, periodic green and blue stripes are seen, likely due to (reoccurring) differently tilted domains within the film (Frka-Petesic et al., 2020), which changes the structural color perceived. Achieving this long-range arrangement puts requirements on the drying step, which is time-dependent as exemplified in Fig. 3d. For example, allowing tactoid annealing prior to kinetic arrest via covered evaporation improves the arrangement (Tran et al., 2018). Here the films were dried differently, and over a period of 1–2 weeks at 20–30 %RH and 19 ± 1 °C, hence there is room for further improvement of the drying step, but this was not investigated here.

3.3. Additional cello-oligosaccharides present in the suspensions

The processing conditions for CNCs, additionally produce cello-oligosaccharides and these can influence the pitch during structural color formation (Bouchard et al., 2016). Therefore, we evaluated the amount and composition of such molecular species present in each fraction type. In a first attempt, the amount of reducing ends was analyzed, as these will increase when species of low degree of polymerization (DP) are present. Reducing ends were found in all three CNC fractions, but evidently, the CNC-H fraction No 1 contained the largest amount of reducing ends, followed by CNC-H fraction No 2 and finally CNC-H fraction No 3 (Fig. 8).

The amount of reducing ends were estimated by an established assay based on 3,5-dinitrosalicylic acid (DNS), during which the aldehyde groups of sugars are oxidized to the respective carboxylic acid (Hostettler, Borel, & Deuel, 1951). Glucose was used for the calibration curve. The DNS assay gives us a first estimate of the amount of reducing ends present. Yet, as described previously, when dealing with sugar mixtures containing sugars with DPs larger than 1, combined with a calibration curve based on glucose, the DNS assay likely overestimates the amount of reducing ends present in the sample (Saqib & Whitney, 2011).

As the low DP cello-oligosaccharides (DPs up to 7) will be dissolved in the CNC suspensions (Bouchard et al., 2016), we additionally used ionic exchange chromatography to assess the composition in solution, results presented in Table 1. The same trend was observed as for reducing ends, i.e. the largest total amount of cello-oligosaccharides was present in the CNC-H fraction No 1, followed by CNC-H fraction No 2 and finally CNC-H fraction No 3.

From the results in both Fig. 8 and Table 1, it is clear that cello-oligosaccharides are present in the samples and the amount is the largest in the CNC fraction No 1. Interestingly, the structural colors of films based on CNC-H fraction No 1 were blue-shifted, when compared to the colors of films based on CNC-H fraction No 2 at similar GLU/CNC ratios, see results in Fig. 4b and d. This is an opposite color trend to the initially anticipated, that is, in the presence of abundant amounts of cello-oligosaccharides, an increasing cello-oligosaccharide amount should result in a red-shift in color. One explanation could be that the cello-oligosaccharide amount is not significant enough in relation to the CNCs. From the results in Fig. 8 we, by assuming all reducing ends come from glucose, roughly estimate that less than <0.077 mg glucose/mg CNC should be present in the CNC-H No 1 suspension – note that the upper limit is an overestimate. Such a low amount is expected to have very little influence on increasing the pitch, compare with the added glucose amounts needed to achieve the respective structural color in Fig. 4. Another hypothesis, explaining the blue shift, could be that at these low concentration the cello-oligosaccharides primarily act as chiral dopants, improving the helical twisting power (reducing the helix pitch, p_0) and that a minute increase in cello-oligosaccharide concentrations (c) results in a blue-shift – this is a typical observation for

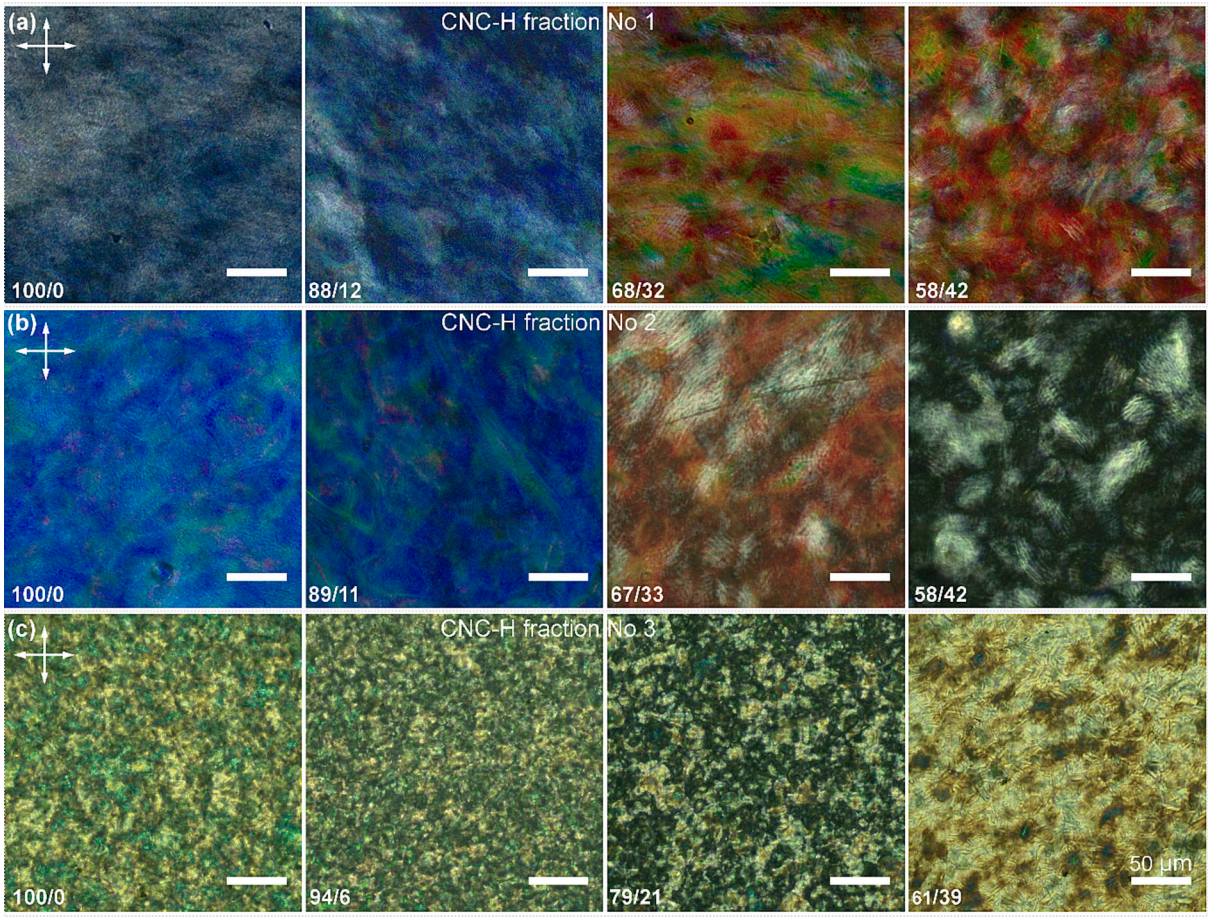

Fig. 6. POM images of CNC-H/GLU films made from varying glucose content and different CNC-H fractions; (a) CNC-H fraction No 1 (CNC/GLU = 100/0, 88/12, 68/32 and 58/42), (b) CNC-H fraction No 2 (CNC/GLU = 100/0, 89/11, 67/33 and 58/42) and (c) CNC-H fraction No 3 (CNC/GLU = 100/0, 94/6, 79/21 and 61/39). All images were attained in reflection mode. Scale bars; 50 µm.

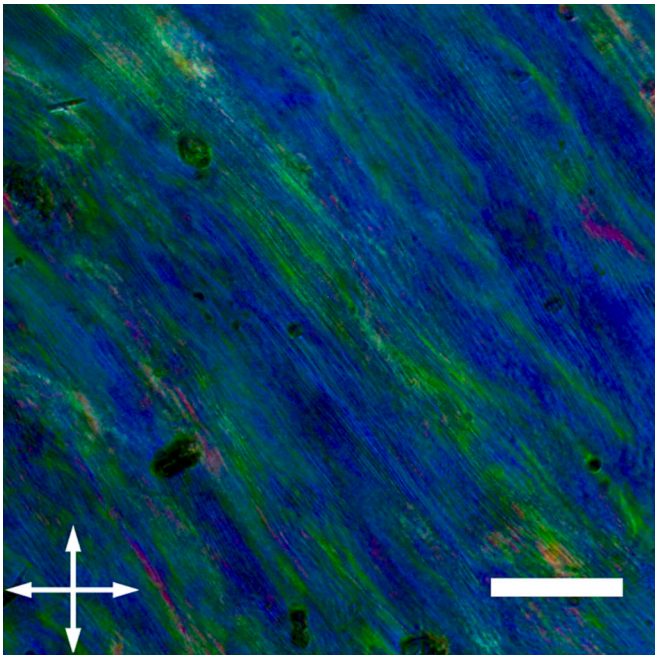

Fig. 7. POM image of the film with CNC-H/GLU composition 79/21. CNC-H fraction No 2. POM attained in reflection mode. Scale bar; 50 µm.

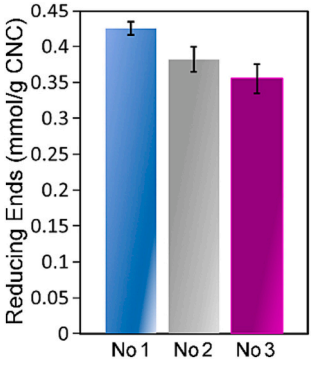

Fig. 8. The amount of reducing ends (mmol/g CNC) varied with the type CNC-H fraction.

thermotropic liquid crystals that shows that, at small concentrations of a chiral dopant in the non-chiral nematic host, the inverse of the pitch is proportional to the concentration of the chiral dopant, i.e. $1 / p_0 \propto c$ (Kitzerow & Bahr, 2001). Indeed, for the neat CNC films, see results for 100/0 films (black lines) in Fig. 4b and d, a blue shift is detected for the film made from CNC-H fraction No 1 compared to that made from fraction No 2. Still, more experimental support is needed to confirm the hypothesis.

Table 1
Mono-, di- and oligo-saccharides present in different CNC-H suspensions.

Mono-, di- and oligosaccharides (μg g^{-1} total dry mass)							
CNC-H	Glucose DP 1	Cellobiose DP 2	Cellotriose DP 3	Cellotetraose DP 4	Cellopentaose DP 5	Cellohexaose DP 6	Total
No 1	280 ± 6	130 ± 0.4	210 ± 30	290 ± 20	170 ± 20	54 ± 10	1140 ± 80
No 2	280 ± 50	73 ± 6	110 ± 10	170 ± 10	99 ± 7	38 ± 1	760 ± 80
No 3	64 ± 3	16 ± 0.6	32 ± 9	71 ± 7	53 ± 4	21 ± 2	260 ± 20

4. Conclusions

The colloidal CNC dispersity causes problems when CNC materials with long-range CNC order and more uniform optical properties and structural colors are desired. Hence, decreasing the dispersity is essential, also, as it can bridge our knowledge gap between the CNC liquid crystal phase and the structure of CNC-based materials. In the classic hydrolysis preparation route, post-processing of CNC suspensions with energy-intense methods are employed to break CNC aggregates and disperse CNCs, but this also shortens CNCs. Additionally, homogenous CNC populations (size, aspect ratio, surface charge) are not necessarily produced. To overcome this, our focus was on the supernatants (denoted fraction No 1 and No 2) that were attained after hydrolysis via centrifugation of the CNC-containing high ionic strength aqueous medium, to show that such supernatants contain very fine CNCs with higher surface charge than the CNCs in the population in the final sediment - in this paper referred to as fraction No 3. The CNCs in the supernatants were longer (300–400 nm on average) than typical wood-based CNCs (≈100–200 nm). A clear difference between the three CNC fractions were seen both in suspension (clarity of suspensions, liquid crystal phase formation with long-range ordering of CNCs with time and increased concentrations, kinetic arrest) and in films (long-range ordering in some cases). Here, structural colors evolved only in films based on CNC fractions No 1 and No 2 and not CNC fraction No 3. Moreover, a clear blue-shift in color was found in films made from CNC fraction No 1 when compared to CNC fraction No 2-based films at similar CNC/GLU compositions, mainly due to more counterions (H^+) present. The extra counterions promote closer packing and, consequently, a reduction of the pitch.

In conclusion, harvesting different CNC fractions immediately after hydrolysis, thereby utilizing the ionic strength of the aqueous medium to facilitate the CNC sedimentation and sorting, presents an alternative way of separating CNCs with different sizes, aspect ratios and surface charges.

CRediT authorship contribution statement

Anna J. Svagan: Conceptualization, Data curation, Formal analysis, Funding acquisition, Methodology, Supervision, Validation, Visualization, Writing – original draft, Writing – review & editing. **Francisco Vilaplana:** Data curation, Methodology, Validation, Writing – review & editing. **Torbjörn Pettersson:** Data curation, Methodology, Validation, Writing – review & editing. **Prasaanth Ravi Anusuyadevi:** Methodology, Validation, Writing – review & editing. **Gunnar Henriksson:** Methodology, Validation, Writing – review & editing. **Mikael Hedenqvist:** Writing – review & editing.

Declaration of competing interest

The authors declare no competing interests.

Data availability

Data will be made available on request.

Acknowledgements

A.J.S. and P.R.A. would like to acknowledge Stiftelsen Olle Engkvist Byggmästare (Grant No. 194-0679) for financial support.

Appendix A. Supplementary data

Supplementary data to this article can be found online at https://doi.org/10.1016/j.carbpol.2023.121723.

References

Abitbol, T., Kam, D., Levi-Kalisman, Y., Gray, D. G., & Shoseyov, O. (2018). Surface charge influence on the phase separation and viscosity of cellulose nanocrystals. *Langmuir, 34*(13), 3925–3933.
Anusuyadevi, P. R., Shanker, R., Cui, Y., Riazanova, A. V., Jarn, M., Jonsson, M. P., & Svagan, A. J. (2021). Photoresponsive and polarization-sensitive structural colors from cellulose/liquid crystal nanophotonic structures. *Advanced Materials, 33*(36), Article e2101519.
Anusuyadevi, P. R., Singha, S., Banerjee, D., Jonsson, M. P., Hedenqvist, M. S., & Svagan, A. J. (2023). Synthetic plant cuticle coating as a biomimetic moisture barrier membrane for structurally colored cellulose films. *Advanced Materials Interfaces, 10*(7), Article 2202112.
Araki, J., & Kuga, S. (2001). Effect of trace electrolyte on liquid crystal type of cellulose microcrystals. *Langmuir, 17*(15), 4493–4496.
Araki, J., Wada, M., Kuga, S., & Okano, T. (2000). Birefringent glassy phase of a cellulose microcrystal suspension. *Langmuir, 16*(6), 2413–2415.
Bai, W., Holbery, J., & Li, K. (2009). A technique for production of nanocrystalline cellulose with a narrow size distribution. *Cellulose, 16*(3), 455–465.
Beck, S., & Bouchard, J. (2014). Auto-catalyzed acidic desulfation of cellulose nanocrystals. *Nordic Pulp & Paper Research Journal, 29*(1), 6–14.
Beck, S., Bouchard, J., & Berry, R. (2011). Controlling the reflection wavelength of iridescent solid films of nanocrystalline cellulose. *Biomacromolecules, 12*(1), 167–172.
Bondeson, D., Mathew, A., & Oksman, K. (2006). Optimization of the isolation of nanocrystals from microcrystalline celluloseby acid hydrolysis. *Cellulose, 13*(2), 171–180.
Bouchard, J., Méthot, M., Fraschini, C., & Beck, S. (2016). Effect of oligosaccharide deposition on the surface of cellulose nanocrystals as a function of acid hydrolysis temperature. *Cellulose, 23*(6), 3555–3567.
Buining, P. A., Philipse, A. P., & Lekkerkerker, H. N. W. (1994). Phase behavior of aqueous dispersions of colloidal boehmite rods. *Langmuir, 10*(7), 2106–2114.
Calvo, V., Álvarez Sánchez, M.Á., Güemes, L., Martínez-Barón, C., Baúlde, S., Criado, A., … Benito, A. M. (2023). Preparation of cellulose nanocrystals: Controlling the crystalline type by one-pot acid hydrolysis. *ACS Macro Letters, 12*(2), 152–158.
Camarero Espinosa, S., Kuhnt, T., Foster, E. J., & Weder, C. (2013). Isolation of thermally stable cellulose nanocrystals by phosphoric acid hydrolysis. *Biomacromolecules, 14*(4), 1223–1230.
de la Torre, J. G., & Bloomfield, V. A. (1981). Hydrodynamic properties of complex, rigid, biological macromolecules: Theory and applications. *Quarterly Reviews of Biophysics, 14*(1), 81–139.
de Souza Lima, M. M., & Borsali, R. (2002). Static and dynamic light scattering from polyelectrolyte microcrystal cellulose. *Langmuir, 18*(4), 992–996.
Dong, X. M., Kimura, T., Revol, J.-F., & Gray, D. G. (1996). Effects of ionic strength on the isotropic–chiral nematic phase transition of suspensions of cellulose crystallites. *Langmuir, 12*(8), 2076–2082.
Dong, X. M., Revol, J.-F., & Gray, D. G. (1998). Effect of microcrystallite preparation conditions on the formation of colloid crystals of cellulose. *Cellulose, 5*(1), 19–32.
Dumanli, A. G., Kamita, G., Landman, J., van der Kooij, H., Glover, B. J., Baumberg, J. J., … Vignolini, S. (2014). Controlled, bio-inspired self-assembly of cellulose-based chiral reflectors. *Advanced Optical Materials, 2*(7), 646–650.
Elazzouzi-Hafraoui, S., Nishiyama, Y., Putaux, J.-L., Heux, L., Dubreuil, F., & Rochas, C. (2008). The shape and size distribution of crystalline nanoparticles prepared by acid hydrolysis of native cellulose. *Biomacromolecules, 9*(1), 57–65.
Evans, D. F., & Wennerström, H. (1999). *The colloidal domain: Where physics, chemistry, biology, and technology meet*. Wiley.
Frka-Petesic, B., Kelly, J. A., Jacucci, G., Guidetti, G., Kamita, G., Crossette, N. P., … Vignolini, S. (2020). Retrieving the coassembly pathway of composite cellulose nanocrystal photonic films from their angular optical response. *Advanced Materials, 32*(19), Article 1906889.

Girard, M., Vidal, D., Bertrand, F., Tavares, J. R., & Heuzey, M.-C. (2021). Evidence-based guidelines for the ultrasonic dispersion of cellulose nanocrystals. *Ultrasonics Sonochemistry, 71*, Article 105378.
Graham, R. M., Lee, D. W., & Norstog, K. (1993). Physical and ultrastructural basis of blue leaf iridescence in two neotropical ferns. *American Journal of Botany, 80*(2), 198–203.
Gray, D. G., & Mu, X. Y. (2015). Chiral nematic structure of cellulose nanocrystal suspensions and films; polarized light and atomic force microscopy. *Materials, 8*(11), 7873–7888.
Hamad, W. Y., & Hu, T. Q. (2010). Structure–process–yield interrelations in nanocrystalline cellulose extraction. *The Canadian Journal of Chemical Engineering, 88*(3), 392–402.
Hamidjaja, R., Capoulade, J., Catón, L., & Ingham, C. J. (2020). The cell organization underlying structural colour is involved in Flavobacterium IR1 predation. *The ISME Journal, 14*(11), 2890–2900.
Honorato-Rios, C., & Lagerwall, J. P. F. (2020). Interrogating helical nanorod self-assembly with fractionated cellulose nanocrystal suspensions. *Communications Materials, 1*(1), 69.
Honorato-Rios, C., Lehr, C., Schütz, C., Sanctuary, R., Osipov, M. A., Baller, J., & Lagerwall, J. P. F. (2018). Fractionation of cellulose nanocrystals: Enhancing liquid crystal ordering without promoting gelation. *NPG Asia Materials, 10*(5), 455–465.
Hostettler, F., Borel, E., & Deuel, H. (1951). Über die Reduktion der 3,5-Dinitrosalicylsäure durch Zucker. *Helvetica Chimica Acta, 34*(6), 2132–2139.
Israelachvili, J. N. (2010). *Intermolecular and surface forces*. Elsevier Science.
Kitzerow, H.-S., & Bahr, C. (2001). *Chirality in liquid crystals*. New York: Springer.
Lagerwall, J. P. F., Schütz, C., Salajkova, M., Noh, J., Hyun Park, J., Scalia, G., & Bergström, L. (2014). Cellulose nanocrystal-based materials: From liquid crystal self-assembly and glass formation to multifunctional thin films. *NPG Asia Materials, 6*(1), e80.
Metzger, C., Drexel, R., Meier, F., & Briesen, H. (2021). Effect of ultrasonication on the size distribution and stability of cellulose nanocrystals in suspension: An asymmetrical flow field-flow fractionation study. *Cellulose, 28*(16), 10221–10238.
Moyroud, E., Wenzel, T., Middleton, R., Rudall, P. J., Banks, H., Reed, A., … Glover, B. J. (2017). Disorder in convergent floral nanostructures enhances signalling to bees. *Nature, 550*(7677), 469–474.
Mu, X., & Gray, D. G. (2014). Formation of chiral nematic films from cellulose nanocrystal suspensions is a two-stage process. *Langmuir, 30*(31), 9256–9260.
Nickerson, R., & Habrle, J. (1947). Cellulose intercrystalline structure. *Industrial and Engineering Chemistry, 39*(11), 1507–1512.
Nordenström, M., Fall, A., Nyström, G., & Wågberg, L. (2017). Formation of colloidal nanocellulose glasses and gels. *Langmuir, 33*(38), 9772–9780.
Onsager, L. (1949). The effects of shape on the interaction of colloidal particles. *Annals of the New York Academy of Sciences, 51*(4), 627–659.
Parker, R. M., Guidetti, G., Williams, C. A., Zhao, T., Narkevicius, A., Vignolini, S., & Frka-Petesic, B. (2018). The self-assembly of cellulose nanocrystals: Hierarchical design of visual appearance. *Advanced Materials, 30*(19), Article 1704477.
Parton, T. G., Parker, R. M., van de Kerkhof, G. T., Narkevicius, A., Haataja, J. S., Frka-Petesic, B., & Vignolini, S. (2022). Chiral self-assembly of cellulose nanocrystals is driven by crystallite bundles. *Nature Communications, 13*(1), 2657.
Pullawan, T., Wilkinson, A. N., & Eichhorn, S. J. (2013). Orientation and deformation of wet-stretched all-cellulose nanocomposites. *Journal of Materials Science, 48*(22), 7847–7855.
Rånby, B., & Ribi, E. (1950). Über den feinbau der zellulose. *Experientia, 6*(1), 12–14.
Reid, M. S., Villalobos, M., & Cranston, E. D. (2017). Benchmarking cellulose nanocrystals: From the laboratory to industrial production. *Langmuir, 33*(7), 1583–1598.
Revol, J. F., Bradford, H., Giasson, J., Marchessault, R. H., & Gray, D. G. (1992). Helicoidal self-ordering of cellulose microfibrils in aqueous suspension. *International Journal of Biological Macromolecules, 14*(3), 170–172.
Saqib, A. A. N., & Whitney, P. J. (2011). Differential behaviour of the dinitrosalicylic acid (DNS) reagent towards mono- and di-saccharide sugars. *Biomass and Bioenergy, 35*(11), 4748–4750.
Schütz, C., Bruckner, J. R., Honorato-Rios, C., Tosheva, Z., Anyfantakis, M., & Lagerwall, J. P. F. (2020). From equilibrium liquid crystal formation and kinetic arrest to photonic bandgap films using suspensions of cellulose nanocrystals. *Crystals, 10*(3), 199.
Tanaka, H., Meunier, J., & Bonn, D. (2004). Nonergodic states of charged colloidal suspensions: Repulsive and attractive glasses and gels. *Physical Review E, 69*(3), Article 031404.
Tatsumi, M., Teramoto, Y., & Nishio, Y. (2015). Different orientation patterns of cellulose nanocrystal films prepared from aqueous suspensions by shearing under evaporation. *Cellulose, 22*(5), 2983–2992.
Tran, A., Hamad, W. Y., & MacLachlan, M. J. (2018). Tactoid annealing improves order in self-assembled cellulose nanocrystal films with chiral nematic structures. *Langmuir, 34*(2), 646–652.
Vignolini, S., Rudall, P. J., Rowland, A. V., Reed, A., Moyroud, E., Faden, R. B., … Steiner, U. (2012). Pointillist structural color in *Pollia* fruit. *Proceedings of the National Academy of Sciences, 109*(39), 15712–15715.
Wang, P.-X., Hamad, W. Y., & MacLachlan, M. J. (2016). Structure and transformation of tactoids in cellulose nanocrystal suspensions. *Nature Communications, 7*(1), Article 11515.
Xiong, R., Singh, A., Yu, S., Zhang, S., Lee, H., Yingling, Y. G., … Tsukruk, V. V. (2020). Co-assembling polysaccharide nanocrystals and nanofibers for robust chiral iridescent films. *ACS Applied Materials & Interfaces, 12*(31), 35345–35353.